Journal of Inorganic and Organometallic Polymers and Materials
https://doi.org/10.1007/s10904-024-03079-3

RESEARCH

Impact of Halide Ion Occupancy on Thermodynamic, Mechanical, Electro-optic, and Electron Transport Characteristics of Rb_2CuAsX_6 (X = F, Cl, Br) Double Perovskites Using Density Functional Theory

Ahmad Ayyaz[1] · G. Murtaza[1] · Youssef Bakkour[2] · Murefah mana Al-Anazy[3]

Received: 24 February 2024 / Accepted: 16 March 2024

Abstract
This work utilizes density functional theory (DFT) to analyze the structural, thermodynamic, mechanical, electro-optic, and electron transport characteristics of Rb_2CuAsX_6 (X = F, Cl, Br) perovskites. The impact of occupancy of different halide ions at the X-site on the thermodynamic, mechanical, optical, and thermoelectric response of studied compounds has also been evaluated. The investigation of the elastic parameters and formation energy has confirmed that the examined perovskites are cubic in structure, stable, and ductile. The thermodynamic characteristics that rely on temperature are estimated using the quasi-harmonic Debye approach. The thermal features such as entropy, heat capacity, and Debye temperature are calculated and analyzed to assess the stability at elevated temperatures and the suitability of compounds for industrial applications. The band structure computations identified Rb_2CuAsF_6, $Rb_2CuAsCl_6$, and $Rb_2CuAsBr_6$ are p-type semiconductors with indirect band gaps of 1.25, 1.10, and 0.83 eV, respectively, which decreases while substituting F with Cl and Br. The optical characteristics such as strong optical absorption ($> 10^5$ cm^{-1}) and minimal dispersion in the visible and ultraviolet spectrum highlight their suitability for solar energy conversion and optoelectronics. Additionally, thermoelectric characteristics have been determined, showing a higher thermoelectric figure of merit (ZT) value of 0.80, 0.79, and 0.78, respectively, at room temperature. Our research anticipates these perovskite combinations exhibit superior photoelectric and thermoelectric efficiency, rendering them potential prospects for advanced photovoltaic and thermoelectric devices.

Keywords Halide double perovskites · DFT · Elastic · Optical properties · Figure of merit

1 Introduction

Presently, with social advancements, there is an increasing tendency towards energy-efficient and environmentally friendly solutions. These technologies have the potential to substitute conventional fossil fuels with carbon-containing alternatives while ensuring a continuous supply of electricity [1, 2]. Scientific societies have expressed curiosity regarding technologies such as solar cells, water splitting, and thermal electricity due to their potential to confront energy concerns [3–5]. Multiple components are now being explored to enhance such technologies, with a specific emphasis on maximizing efficiency, and functionality, and reducing environmental harm. Currently, experimentally and theoretically evidenced double perovskites are widely regarded as adaptable materials, as a consequence of their diverse range of uses [6–8]. Double perovskite compounds have recently attracted significant interest owing to their prospective uses in several fields, such as LEDs, radiation detectors, photovoltaic cells, sensors, fuel cell technology, thermal electricity, catalytic activity, and various other fields [9–13]. Over the last two decades, a notable surge in concern regarding the production of perovskite solar cells has developed because of their excellent performance and cost-effectiveness. The experimentally achieved power conversion efficiency has increased

✉ Ahmad Ayyaz
raiayyaz23@gmail.com

✉ G. Murtaza
gmrai@gcu.edu.pk

[1] Centre for Advanced Studies in Physics, GC University Lahore, Lahore 54000, Pakistan

[2] Department of Radiological Sciences, College of Applied Medical Sciences, King Khalid University, Abha, Saudi Arabia

[3] Department of Chemistry, College of Sciences, Princess Nourah bint Abdulrahman University (PNU), P.O. Box 84428, Riyadh 11671, Saudi Arabia

Published online: 06 May 2024

from 3.8% in 2009 to 25.5% in 2021. These unique qualities allowed it to exceed the performance of traditional thin-film solar cells [14–16], because of its adequate bandgap, superior absorption coefficient, and almost identical effective masses of charge carriers [17]. The lead-based perovskite combinations are toxic and unstable in long-term exposure to humidity, light, and heat, which hinders their integration into innovative technological applications [18–20].

Halide-based double perovskites, represented by the formula $A_2M^+M^{3+}X_6$, have become a promising alternative to lead-based perovskites for use in photovoltaic cells [21], electronic components [22], and thermoelectric systems [23]. These perovskites offer the capability for improved stability and decreased toxicities while yet retaining high performance. Various experimental and computational investigations are being carried out on Cs-based perovskite materials with the chemical formula $Cs_2M^+M^{3+}X_6$ (where $M^+ = Ag^+$, Ga^+, Cu^+, etc., $M^{3+} = Bi^{3+}$, In^{3+} and $X = Cl^-$, Br^-, I^-). McClure et al. researched Cs_2AgBiX_6 (X = Cl, Br), which had band gaps of 2.7 eV and 1.9 eV, respectively. Nevertheless, these bandgaps are above the Shockley–Queisser band gap threshold for the most efficient solar cells, leading to a decreased efficiency of approximately 2.5%. Furthermore, $Cs_2AgBiBr_6$ has been demonstrated to be unstable when subjected to ambient air and light for an extended period [24, 25]. Therefore, it is advantageous to investigate the advancement of double perovskites because of their exceptional potential. Several scientists have done computational research to investigate the electrical, optical, and thermoelectric properties of different perovskite materials [26, 27]. Cs_2YAuX_6 (X = Cl, Br) [28] and Cs_2TlAsX_6 (X = Cl, Br, I) [29] have been identified as feasible materials for solar energy and optoelectronic applications due to their appropriate band gaps, low effective masses, strong light absorption, and low reflectivity. Moreover, several combinations Rb_2CuBiX_6 (Cl, Br) [30], Cs_2AgAsX_6 (X = Cl, Br, I), Rb_2AgAsX_6 (X = Cl, Br, I) [31], and Na_2AgAsX_6 (Cl, Br) [32] have been explored having higher absorbance and higher figure of merit values, which suggest their capability for renewable energy production. These investigations provide valuable insights into the chemical element combinations used in perovskite materials and motivated us to explore novel combinations containing copper (Cu) and arsenic (As) as two monovalent and trivalent cations. This stable combination might have exceptional electro-optic and electron transport features.

The primary aim of the current study is to forecast novel materials with improved optoelectronic and electron transport characteristics using density functional theory for energy technology. This paper examines the structural stability, thermodynamic, elastic, electro-optic, and thermoelectric properties of the Rb_2CuAsX_6 (X = F, Cl, Br) perovskites. This article also highlights the impact of different halide ion occupancies on the aforementioned properties. The materials Rb_2CuAsX_6 (X: F, Cl, Br), as far as we are aware, have not been the focus of any theoretical or experimental investigation. We expect that our research will provide essential insights for forecasting lead-free double perovskite materials suitable for upcoming thermoelectric devices and solar energy harvesting.

2 Methodology

The perovskites Rb_2CuAsX_6 (X = F, Cl, Br) were analyzed using the Wien2k code. This code is based on the principles and concepts of density functional theory, which are implemented using the full potential linearized augmented plane wave (FP-LAPW) approach [33]. The wave function of an electron gas has been determined in relation to the electron density using the Schrödinger wave equation. The spherical and plane wave solutions are allocated to the muffin-tin and interstitial areas by maintaining a constant potential in each zone. The structural analysis used the Perdew–Burke–Ernzerhof generalized gradient approximation (PBE-GGA) to optimize the structures and accurately determine the ground state components [34]. This approach undervalues the band gap and electronic behavior. The Tran–Blaha modified Becke–Johnson (TB-mBJ) potential, known for its versatility and excellent accuracy, was applied over the calculations of PBE-GGA to adjust the band gap [35]. This adjustment is especially beneficial for improving the accuracy of bandgap estimates in materials where there is a significant impact of dominant electron–electron interactions [36]. The G_{max} (Gaussian factor) and ℓ (angular momentum) were set at 8.0 and 10, respectively, which are key criteria for software to manage program execution. The energy convergence of the precise Hamiltonian of the structure is achieved by setting the muffin-tin radius (R_{MT}) and wave vector product to 10. The k-mesh order is another feature that might influence convergence. The k-points are chosen in a 20 × 20 × 20 grid to create a dense mesh that converges the energy to within 0.01 mRy. The optical investigation was conducted using the Kramer–Kronig relation [37], whereas the thermoelectric study was performed using the BoltzTraP code [38]. Moreover, thermodynamic aspects were calculated by using the GIBBS2 code [39]. An appropriate R_{MT} radius aims to reduce the overlapping of muffin-tin spheres between neighboring atoms. This gap is essential for accurately representing atom-atom interactions and positioning electrons in close proximity to atoms [26]. The R_{MT} values for constituents Rb, Cu, As, and X (F, Cl, Br) were selected as 2.0, 1.6, 1.9, and 1.8, respectively.

3 Results and Discussion

3.1 Structure and Stability

The structural features of Rb_2CuAsX_6 (X = F, Cl, Br) compounds have been optimized in the cubic phase with space group Fm-3m using the PBE-GGA functional method, which is crucial for improving the long-term stability of the compounds being analyzed [40, 41]. The overall energy of the double perovskite being examined is equal to the system's lowest energy state. The Murnaghan equation of state is a commonly used mathematical model in materials science to explain the relationship between a crystal lattice's volume and its total energy. It gives a clear and precise explanation of the relation between the equilibrium lattice parameter, volume, energy, and bulk modulus. The lattice parameters are optimized using the Murnaghan equation of state to analyze the anticipated energy curve (E_{Total}) and determine key parameters including equilibrium lattice parameter, ground state volume (V_0), and ground state energy (E_0) by the relation [42]:

$$E(V) = E_0(V) + \left[\frac{B_0 V}{B_0'(B_0'-1)}\right] \times \left[B_0\left(1-\frac{V_0}{V}\right) + \left(\frac{V_0}{V}\right)^{B_0'} - 1\right] \quad (1)$$

The cubic arrangement of Rb_2CuAsX_6 (X = F, Cl, Br) with space group Fm-3m is displayed in Fig. 1. Perovskites' structure and stability may be better understood by the Goldsmith tolerance parameter, which accounts for the effect of different cation sizes at the A and B locations. It allows us to determine if a specific combination of ions may produce a flawless perovskite structure, or whether particular defects and instabilities are more likely to occur. The stability of the structure linked to the Goldsmith tolerance factor (τ) is calculated using the formula [43]:

$$\tau = \frac{r_{Rb} + r_X}{\sqrt{2}\left(\frac{r_{Cu}+r_{As}}{2} + r_X\right)} \quad (2)$$

where r_{Rb}, r_X, r_{Cu}, and r_{As} represent the ionic radii of Rb, X (F, Cl, Br), Cu, and As atoms, respectively. The material maintains a stable cubic perovskite structure within a tolerance factor range of 0.7 to 1.11 [44]. The optimized double perovskite's total energy changing with volume is presented in Fig. 2, while Table 1 presents the calculated equilibrium features of investigated materials. The tolerance factor values of Rb_2CuAsX_6 (X = F, Cl, Br) suggest that their composition is stable, as given in Table 1.

Thermal stability has been confirmed by the computation of formation energy (E_F) as well as Gibbs free energy (G) [45], E_F is determined using the formula [46]:

$$E_F = E_{Rb_2CuAsX_6} - \left(2E_{Rb} + E_{Cu} + E_{As} + 6E_X\right) \quad (3)$$

Moreover, thermal stability is further verified by the negative values of Gibbs free energy resulting from excess energy given up bringing the structure towards equilibrium. The values of E_F and G are given in Table 1 which ensures that the studied materials are thermally stable.

3.2 Thermodynamic Properties

The thermodynamic characteristics that rely on temperature are estimated using the quasi-harmonic Debye approach [47–49]. Since the quasi-harmonic Debye concept is completely valid throughout the temperature range of 0 to 600 K, Figure 3 displays the volume (V), bulk modulus (B), entropy

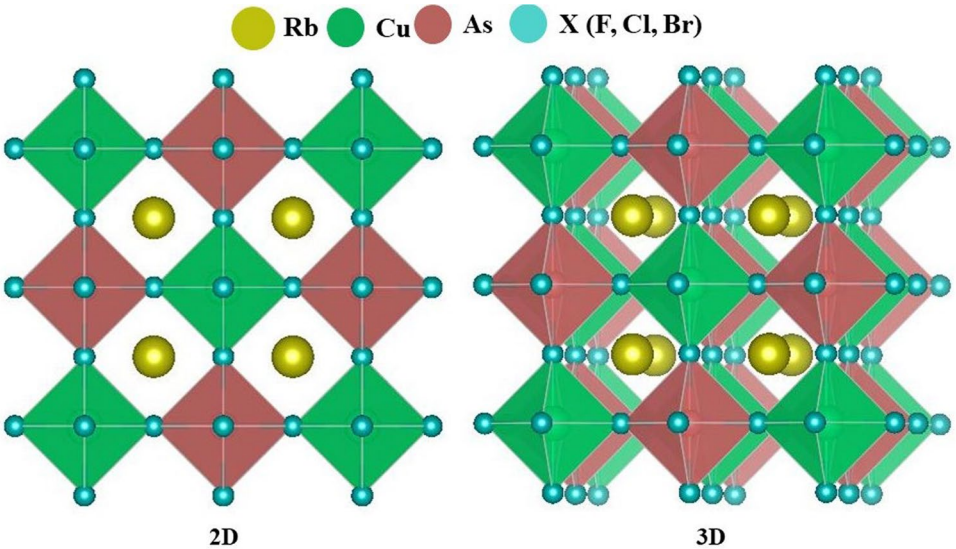

Fig. 1 FCC structure in 2D and 3D for Rb_2CuAsX_6 (X = F, Cl, Br)

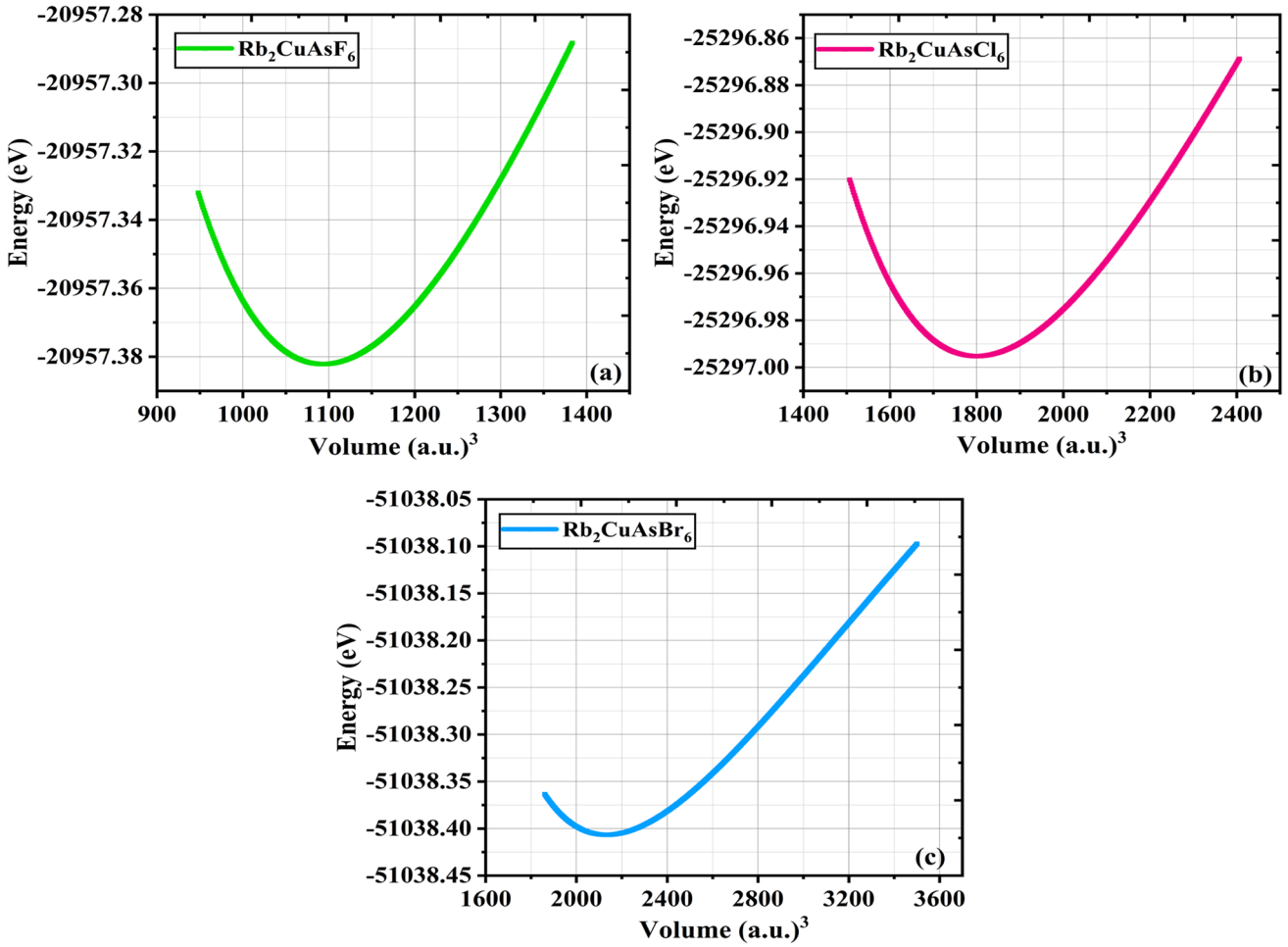

Fig. 2 Optimization graphs showing energy versus volume curves of Rb_2CuAsX_6 (X = F, Cl, Br)

Table 1 Optimized values of structural and stability aspects of Rb_2CuAsX_6 (X = F, Cl, Br)

Structural parameters	Rb_2CuAsF_6	$Rb_2CuAsCl_6$	$Rb_2CuAsBr_6$
Lattice constant (Å)	8.65	10.22	10.82
Volume at ground state (V_0)	1093.8052	2567.9356	2625.5596
Ground state energy (E_0)	− 116,238.4615	− 108,913.8384	− 143,699.4665
Bulk modulus (B)	56.55	31.71	25.67
Bulk modulus derivative	5.0	5.0	5.0
Tolerance factor (τ)	0.93	0.96	0.83
E_f (eV atom^{-1})	− 1.37	− 1.22	− 1.05
G (KJ mol^{-1})	-2.75×10^7	-3.32×10^7	-6.7×10^7

(S), molar specific heat (C_P), and Debye temperature (θ_D) for Rb_2CuAsX_6 (X = F, Cl, Br).

The correlation between volume and temperature for Rb_2CuAsX_6 (X = F, Cl, Br) is justified in Fig. 3a. The volume of the observed three materials varies directly with temperature due to the expansion of material with increasing temperature. Meanwhile, the bulk modulus follows a downward trend with an increase in temperature for the investigated materials. The variation in bulk modulus with temperature may be due to the fact that temperature causes an expansion in the separation between atoms, leading to an increased unit cell volume and therefore a drop in bulk modulus. The inverse correlation of B with temperature is plotted in Fig. 3b. Therefore, based on the B values at 300 K, it is evident that Rb_2CuAsF_6 would exhibit greater stiffness in comparison to the $Rb_2CuAsCl_6$

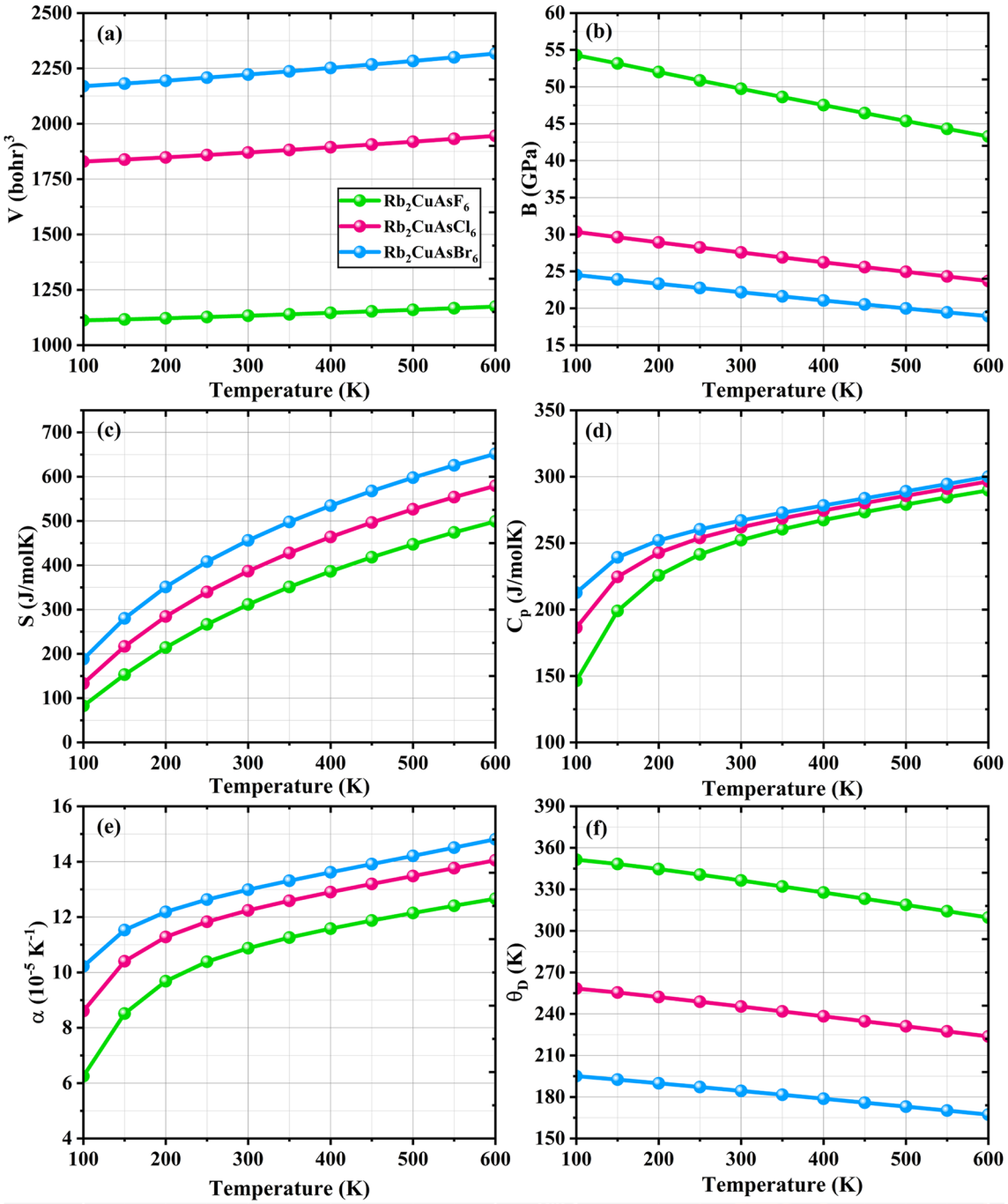

Fig. 3 Variation against temperature in **a** volume **b** bulk modulus **c** entropy **d** specific heat **e** thermal expansion **f** Debye temperature for Rb_2CuAsX_6 (X = F, Cl, Br)

and $Rb_2CuAsBr_6$. Entropy (S) is an inherent attribute that quantifies the degree of disturbance or randomness inside a system's structure [50]. Figure 3c illustrates the relationship between entropy and temperature. It shows a proportional rise in entropy at temperatures above 100 °C, indicating an improvement in structural irregularity. The values of S are found to be higher for $Rb_2CuAsBr_6$ than Rb_2CuAsF_6 and $Rb_2CuAsCl_6$ showing greater disorder in $Rb_2CuAsBr_6$.

Furthermore, the relationship between specific heat at a fixed pressure (C_P) and temperature is illustrated in Fig. 3d. This parameter is crucial in thermodynamics since it offers insights into vibrational characteristics, phase transitions, and other related aspects [51]. The figure illustrates a quick

rise in the value of C_P at lower temperature values ranging from 0 to 200 K, while beyond 200 K, there is a steady rise in C_P. At a temperature of 300 K, the computed specific heat capacity was 241.52 J mol^{-1} K^{-1}, 253.88 J mol^{-1} K^{-1}, and 260.45 J mol^{-1} K^{-1} for Rb_2CuAsF_6 and $Rb_2CuAsCl_6$, and $Rb_2CuAsBr_6$, respectively. Furthermore, Fig. 3e displays the relationship between the thermal expansion coefficient α and temperature. The thermal expansion coefficient offers important information on the interatomic bonding and melting temperature of material [52]. The data shows that the value of α grows as the temperature rises. The rate of increase in α is faster at low temperatures (up to 200 K) and slower at high temperatures (beyond 200 K).

The slow growth of α above 200K is because α becomes saturated at this temperature. The room temperature (300 K) values of α are 10.87 K^{-1}, 12.24 K^{-1}, and 12.98 K^{-1}, respectively, for Rb_2CuAsF_6, $Rb_2CuAsCl_6$, and $Rb_2CuAsBr_6$. A lower value of α for Rb_2CuAsF_6 in comparison to the $Rb_2CuAsCl_6$ and $Rb_2CuAsBr_6$ indicates stronger bonding, resulting in a greater melting temperature. The Debye temperature (θ_D) is used to describe the activation of phonons and assess different lattice thermal features and the suitability of compounds for industrial applications. Higher θ_D leads to increased energy phonon modes by hindering the soft phonon mode lacking radiation relaxation, resulting in increased emission of photons. Conversely, lower θ_D, which typically includes a higher soft phonon mode, can facilitate non-radiative relaxation [52]. Rb_2CuAsF_6 has a higher θ_D of 336 K at 300 K, compared to $Rb_2CuAsCl_6$ and $Rb_2CuAsBr_6$ which have 245.39 K and 184.39 K, as shown in Fig. 3f.

3.3 Elastic Properties

3.3.1 Elastic Constants and Mechanical Stability

Elastic constants are physical characteristics used to assess the mechanical stability as well as durability of a solid and to identify its brittle or ductile nature. Knowledge of elastic constants is crucial for evaluating a solid's suitability for mechanical and engineering purposes [53]. Elastic constants (C_{ij}) for the three double perovskites Rb_2CuAsX_6 (X = F, Cl, Br) are found using density functional theory (DFT) and are listed in Table 2. The three distinct elastic stiffness coefficients, C_{11}, C_{12}, and C_{44}, obtained by density functional theory (DFT), meet the necessary conditions for mechanically stable cubic structures. The conditions are stated as follows: C_{11} must exceed the absolute magnitude of C_{12}, $C_{11} + 2C_{12}$ must be positive, and C_{44} should exceed zero according to the Born elastic stability criterion [54–57]. As a result, the Born criterion states that the double perovskites Rb_2CuAsX_6 (X = F, Cl, Br) are mechanically stable. Specific mechanical parameters like bulk modulus (B), Young's modulus (Y), and shear modulus (G) may be determined using the following formulae:

$$B = \frac{C_{11} + 2C_{12}}{3} \tag{4}$$

$$Y = \frac{9BG_V}{3B + G_V} \tag{5}$$

$$G = \frac{\left(G_V + G_R\right)}{2} \tag{6}$$

The calculations show that the bulk modulus (B) for the compound Rb_2CuAsF_6 is 55.77, which is greater than that of $Rb_2CuAsCl_6$ (31.43) and $Rb_2CuAsBr_6$ (25.46), as reported in Table 2. When these compounds are compressed from each direction, Rb_2CuAsF_6 shows more resistance to the changes in volume than $Rb_2CuAsCl_6$ and $Rb_2CuAsBr_6$. The shear modulus (G) is a key parameter that defines the resistance to stress of a material. The shear modulus measurements indicate that Rb_2CuAsF_6 has a greater shear modulus (20.66) compared to $Rb_2CuAsCl_6$ (10.89) and $Rb_2CuAsBr_6$ (8.44). The findings show that Rb_2CuAsF_6 has better hardness and stronger resistance against deformation than $Rb_2CuAsCl_6$ and $Rb_2CuAsBr_6$. The Young modulus (Y) is a quantity that defines the intrinsic stiffness of a certain material. According to Table 2, the data clearly shows that Rb_2CuAsF_6 has also a larger value of Y (55.17) compared to $Rb_2CuAsCl_6$ (29.28) and $Rb_2CuAsBr_6$ (22.77), suggesting that Rb_2CuAsF_6 has more stiffness. The Poison ratio (υ) offers vital information on a material's mechanical characteristics, including its ductility or brittleness. Materials having a Poisson's ratio (υ) above 0.26 are categorized as ductile, while materials with a Poisson's ratio less than 0.26 are regarded as brittle. The investigation found that the value of υ is above 0.26 for all materials [58]. The results concerning υ indicate that the materials being studied display ductile properties. The B/G ratio, often known as Pugh's criterion, is a measure also used to assess ductility or brittleness. According to Pugh's criterion, a material is considered ductile if the ratio of bulk modulus (B) to shear modulus (G)

Table 2 Elastic stiffness coefficients, elastic moduli, Pugh's ratio, and anisotropy of Rb_2CuAsX_6 (X = F, Cl, Br)

Compounds	C_{11} (GPa)	C_{12} (GPa)	C_{44} (GPa)	B (GPa)	G (GPa)	Y (GPa)	B/G	υ	A
Rb_2CuAsF_6	106.83	30.24	13.59	55.77	20.66	55.17	2.69	0.33	0.35
$Rb_2CuAsCl_6$	51.79	21.25	8.66	31.43	10.89	29.28	2.88	0.34	0.56
$Rb_2CuAsBr_6$	38.46	18.92	7.63	25.46	8.44	22.77	3.01	0.35	0.78

surpasses 1.75, and it is classed as brittle if the B/G ratio gets lower than 1.75 [59]. This criterion also verifies the ductile or flexible nature of all compounds since the B/G ratio is greater than 1.75.

3.3.2 Anisotropic Properties

Microscopic fractures in a material may be identified by analyzing its anisotropic characteristics. The anisotropic factor (A) evaluates the structural homogeneity or variation of a material across different orientations and is determined by a formula:

$$A = \frac{2C_{44}}{C_{11} - C_{12}} \tag{8}$$

When A = 1, the medium is termed isotropic; however, if $0 < A < 1$ or $A > 1$, then the material is regarded as anisotropic [60]. The values of A indicate that the materials being studied exhibit anisotropic behavior.

To examine anisotropy, Fig. 4 shows three-dimensional visualizations of Young's modulus of a single crystal along certain crystallographic orientations for Rb_2CuAsX_6 (X = F, Cl, Br). Materials used for advanced manufacturing and engineering fields need to possess substantial anisotropy. The graphs were created using the SC-EMA approach [61–63] and were derived from computations. Both the color scheme and the axes depict Young's modulus in GPa showing a strong association with the direction. All directional surfaces obtained show significant deformations compared to a spherical shape, confirming that mechanical properties vary with direction and indicating

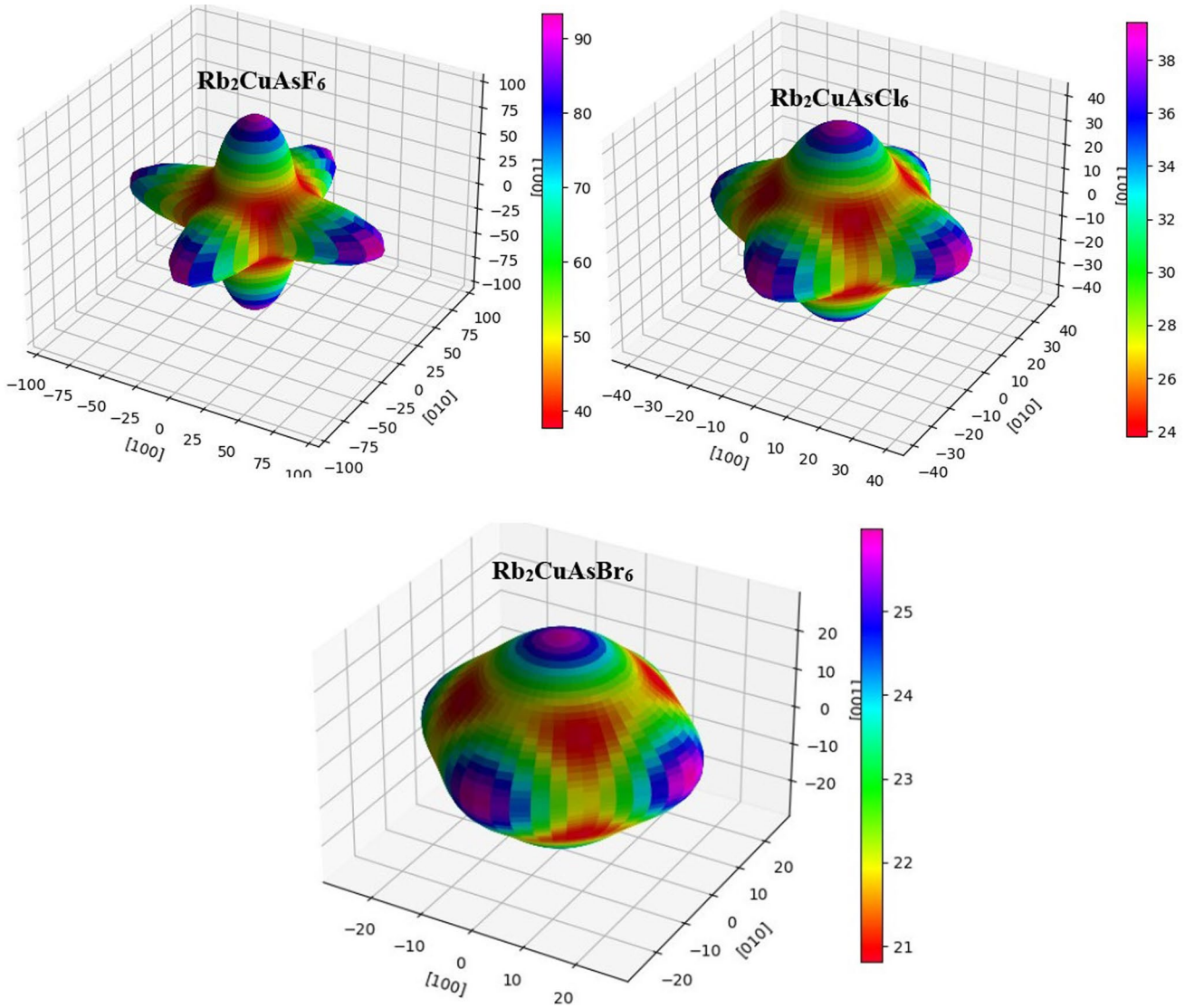

Fig. 4 Young's modulus in 3D along various orientations for Rb_2CuAsX_6 (X = F, Cl, Br)

the strong elastic anisotropy of the materials studied. For the materials under study, the anisotropy level decreases in the order: Rb_2CuAsF_6 > $Rb_2CuAsCl_6$ > $Rb_2CuAsBr_6$. Moreover, the highest Young's modulus value is in the [100], [010], and [001] orientations decreasing in a similar order: Rb_2CuAsF_6 > $Rb_2CuAsCl_6$ > $Rb_2CuAsBr_6$, indicating that stiffness is decreasing along with anisotropy. These outcomes suggest greater mechanical strength and anisotropy in Rb_2CuAsF_6 than in $Rb_2CuAsCl_6$ and $Rb_2CuAsBr_6$.

3.4 Electronic Properties

This study analyzed the electronic features of Rb_2CuAsX_6 (X = F, Cl, Br) by computing the band structure, total density of states (TDOS), and partial density of states (PDOS). The band structures have been determined by applying two approaches (PBE-GGA, and TB-mBJ approximation) due to the absence of prior experimental as well as theoretical data for comparison, in order to strengthen the validity of our findings [64].

The band energies are computed using PBE-GGA and TB-mBJ potentials to illustrate the band configuration. The band gap (E_g) values are calculated at the W, X, L, K, and Γ symmetric locations using PBE-GGA**,** as mentioned in Fig. 5. The E_g values using the PBE-GGA framework are underestimated and found to be 0.97, 0.59, and 0.26 eV. Moreover, the computation has been improved using the TB-mBJ approximation, as shown in Fig. 6, along the high-order symmetry directions W, X, L, K, and Γ for Rb_2CuAsF_6, $Rb_2CuAsCl_6$, and $Rb_2CuAsBr_6$. The standard band gap values increased to 1.25 eV for Rb_2CuAsF_6, 1.10 eV for $Rb_2CuAsCl_6$, and 0.83 eV for $Rb_2CuAsBr_6$. This boost is due to the TB-mBJ exchange potential pushing the conduction bands composed of specific electronic states, beyond the Fermi level. The band gap values of the current materials drop as the halide ionic size increases from F to Br, as seen in Table 1. Due to the smaller ionic radius of Br compared to Cl and F, replacing Br with Cl and F results in a red shift in the band gap. Therefore, this implies that the examined materials are suitable for application in optoelectronics, photovoltaics, and energy-harvesting devices.

The patterns of TDOS show uniform densities as well as band gaps confirmation of the analyzed perovskites. The total density of states (TDOS) below the Fermi level (E_F) is higher than in the conduction band (CB), suggesting a p-type conductivity. Furthermore, the significant variation in the highest valence band along L–Γ–X results in a low effective mass for the holes, leading to strong mobility and exhibiting p-type conductivity. The states in the highest valence band along X–W–K are partially flat, indicating the presence of a low-occupied orbital at the Fermi level. This may also be associated with the comparatively large effective mass of holes [65].

Partial densities of states (PDOS) are analyzed to understand the contributions of Rb, Cu, As, and X elements to the valence bands (VBs) and conduction bands (CBs), aiding in the full assessment of the electronics structure's impact on device functionality. The outcomes obtained from the TB-mBJ potential are shown in Fig. 7. The PDOS is important in governing the possible electronic transitions among specific energy levels. The PDOS pattern indicates that the valence bands and conduction bands borders are mainly made up of Cu-*d* and As-*p* orbitals, respectively. Halides (F, Cl, Br) little contributions were seen in the deep area of the valence band, although they do not affect the electronic behavior. Rb has a non-resistant role in forming the frontier bands by just

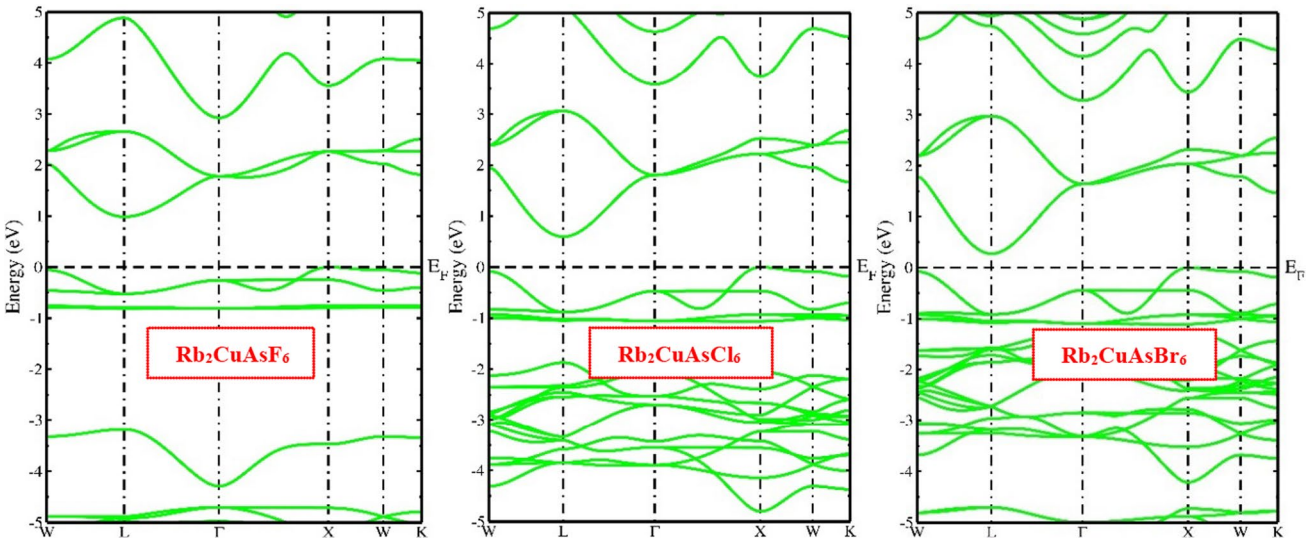

Fig. 5 The band structures of Rb_2CuAsX_6 (X = F, Cl, Br) using PBE-GGA approximation

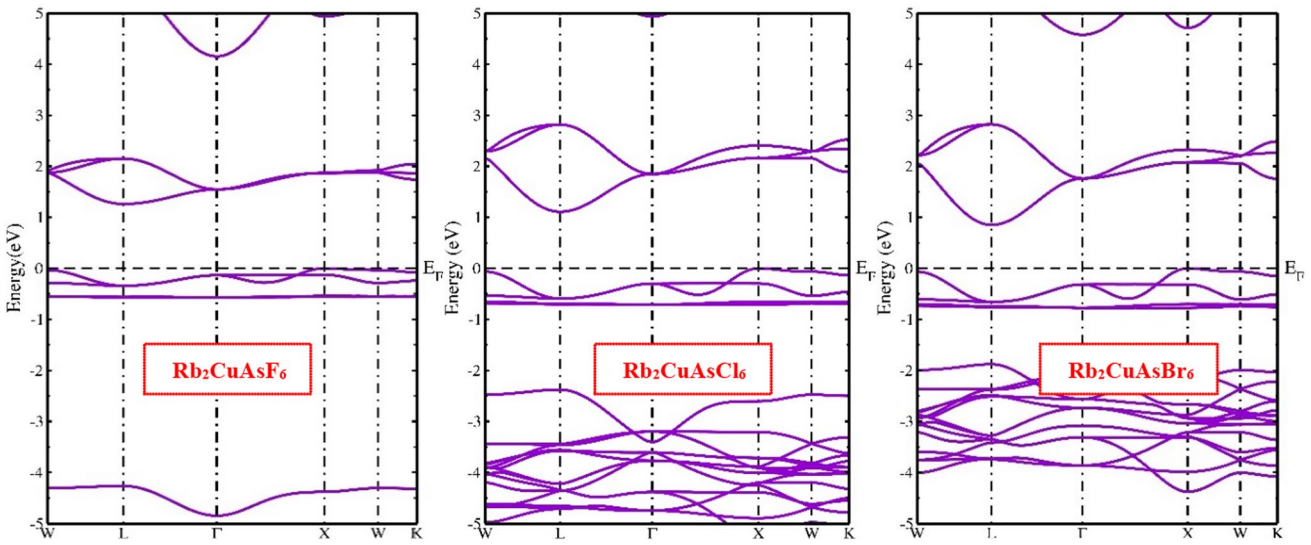

Fig. 6 The band structures of Rb_2CuAsX_6 (X = F, Cl, Br) using TB-mBJ approximation

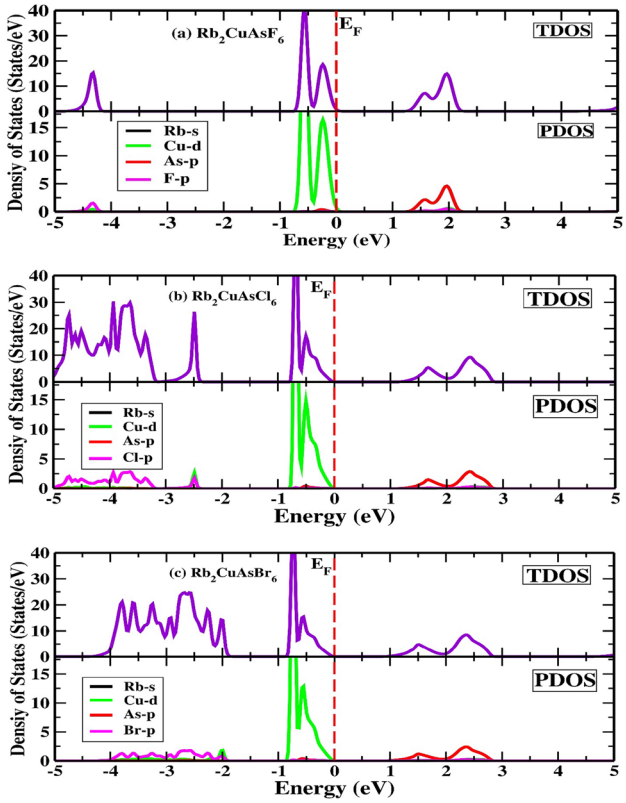

Fig. 7 The computed density of states of Rb_2CuAsX_6 (X = F, Cl, Br) using TB-mBJ

donating charges to sustain structural stability [65]. The bottom of the conduction band is mostly due to As-*p*, whereas the top of the valence band includes Cu-*d* states. Figure 7a–c shows that the influence of the As-*p* reduces progressively from F to Br. The replacement of Br with I induces a red shift in the I-5*p* and Sb-5*p* states in the conduction band, resulting in a red-shifted band gap. Increasing atomic radius decreases the coulombic attraction of the nucleus on valence shell electrons, causing a reduction in the band gap energy. Therefore, the findings of electronic properties provide evidence of the fact that Cu-*d* and As-*p* states play vital contributions to electronic transitions, which dictate the optical and thermoelectric attributes of the studied materials.

3.5 Optical Properties

The optical properties of studied materials are mainly determined by the interaction between matter and light and the characteristics of the energy gap. This paper provides a detailed description of the optical characteristics of Rb_2CuAsX_6 (X = F, Cl, Br) double perovskites in relation to the dielectric function, by employing the TB-mBJ potential. The dielectric function, commonly known as the permittivity of a material, is determined by the relation [66]:

$$\varepsilon(\omega) = \varepsilon_1(\omega) + i\varepsilon_2(\omega) \tag{9}$$

The real portion $\varepsilon_1(\omega)$ represents the generated polarization caused by the interaction between light and the material, whereas the imaginary part $\varepsilon_2(\omega)$ indicates the capacity of attenuation of light that is transmitted via material. The relationship between several associated optical characteristics such as refractive index n (ω), reflectivity R (ω), optical absorption coefficient α (ω), optical energy loss function L (ω), and optical conductivity σ (ω) is analyzed based on $\varepsilon_1(\omega)$ and $\varepsilon_2(\omega)$ [67, 68].

The calculated energy-dependent $\varepsilon_1(\omega)$ of Rb_2CuAsX_6 (X = F, Cl, Br) in Fig. 8a shows a relatively weak energy dependency at minimal energy. For Rb_2CuAsF_6, $Rb_2CuAsCl_6$, and $Rb_2CuAsBr_6$, the static values of $\varepsilon_1(\omega)$ are 3.40, 4.24, and 5.13, respectively. The rising order of halides from F to Br exhibits an increase in $\varepsilon_1(0)$, indicating that heavier halogens become increasingly optically polarizable. The observed increase in $\varepsilon_1(0)$ promotes a reduced recombination rate of energy carriers, enhancing the efficiency of optical components. The value of this parameter is negatively correlated with electronic band gap energy as shown by the Penn model [69]: $\varepsilon_1(0) = 1 + (\hbar\omega_p/E_g)^2$. In the visible range, the main peaks of $\varepsilon_1(\omega)$, which are linked to the highest propagation of light, are found at the resonance frequencies. Beyond the resonance limit, the $\varepsilon_1(\omega)$ decreases rapidly with several relaxation peaks associated with electronic inter-band transitions. The relaxation time may be calculated from the peak frequency using the formula: $\tau_r = 1/\omega = \hbar/E$. $Rb_2CuAsBr_6$ has a higher peak in the visible area compared to $Rb_2CuAsCl_6$ and Rb_2CuAsF_6 due to its smaller band gap energy. Moreover, at the energy values of 2.08 eV, $\varepsilon_1(\omega)$ is less than 0, Rb_2CuAsF_6 displays metallic properties with complete reflection. Within this energy range, the frequency of the incoming radiation exceeds the plasma frequency. However, $Rb_2CuAsCl_6$ and $Rb_2CuAsBr_6$ show no reflection throughout the energy range.

Figure 8b demonstrates that $\varepsilon_2(\omega)$ stays at zero for photons with energy below the band gap energy for both substances, suggesting insufficient energy for electronic inter-band transition. Furthermore, the $\varepsilon_2(\omega)$ rises from the threshold levels to the peak value of 7.27 (at 1.80 eV), 6.33 (at 1.94 eV), and 5.53 (at 2.05 eV) for Rb_2CuAsF_6, $Rb_2CuAsCl_6$, and $Rb_2CuAsBr_6$, respectively. The multi-peak phenomena seen in the observed energy regions are caused by the varying rates of possible electronic transitions from Cu-*d* states in the VB to the As-*p* states in the CB. Moreover, a decrease in peak intensity can be attributed to the decreased PDOS by replacing F with Cl and Br (refer to Fig. 6). Thus, it is evident that Rb_2CuAsX_6 (X = F, Cl, Br) exhibits varying optical absorption capacities throughout a wide range of electromagnetic frequencies. The large peak magnitudes seen usually facilitate the

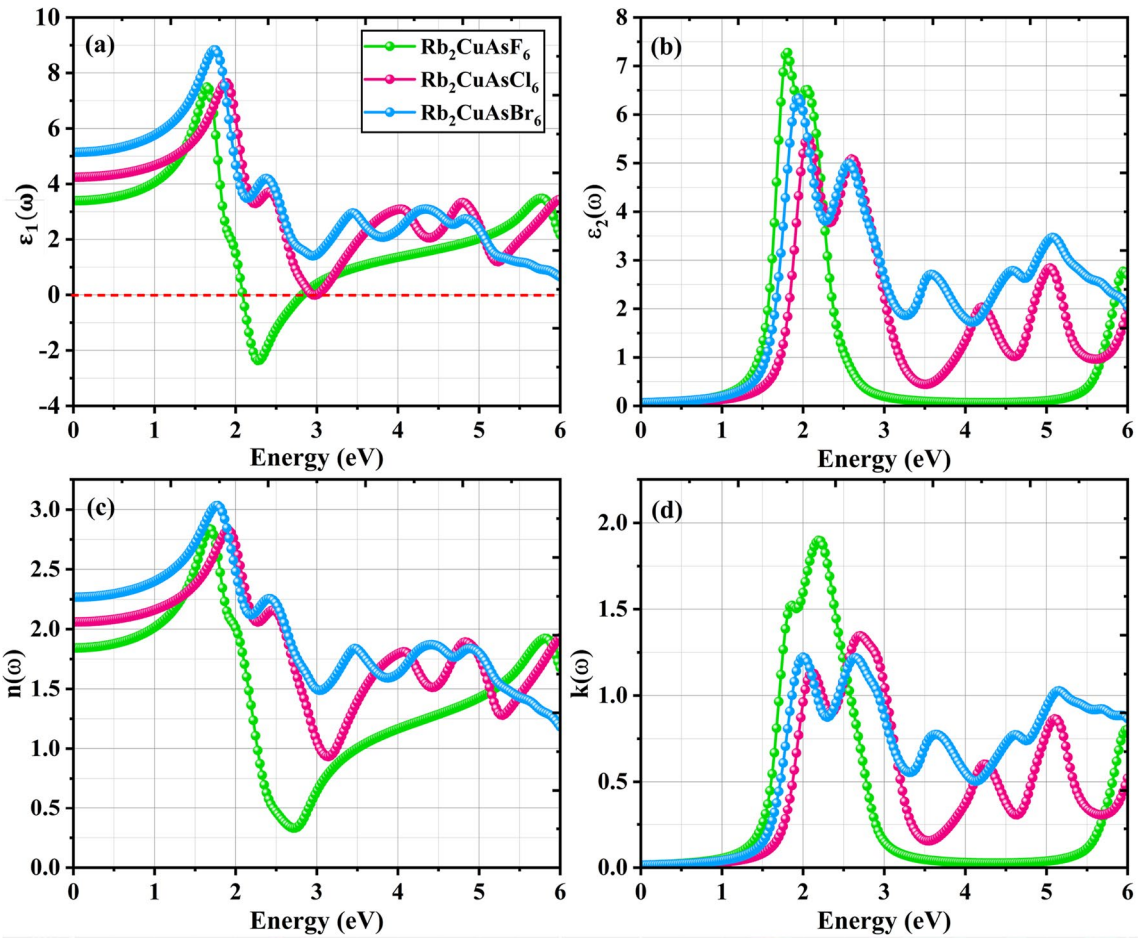

Fig. 8 Variation in optical parameters **a** $\varepsilon_1(\omega)$ **b** $\varepsilon_2(\omega)$ **c** $n(\omega)$ **d** $k(\omega)$ with energy for Rb_2CuAsX_6 (X = F, Cl, Br)

extension of polarized electrons into conducting states, hence improving the efficiency of photovoltaic conversion. Based on this discussion, the ideal operating areas in the visible and ultraviolet spectrums make the materials very suitable for photovoltaic (PV) conversion and optoelectronic devices.

The transparent nature of Rb_2CuAsX_6 (X = F, Cl, Br) is primarily dictated by its optical refractive index n(ω). It measures the amount of bending of light as it travels through a substance. Assessing this characteristic is crucial for the precise use of materials in optical devices. Figure 8c shows that the refractive index at zero frequency appears to be 1.84, 2.05, and 2.26, for Rb_2CuAsF_6, $Rb_2CuAsCl_6$, and $Rb_2CuAsBr_6$. The rise in n(0) by shifting from F to Br occurs due to the red-shifted band gaps. Furthermore, these values are linked to $\varepsilon_1(0)$ in the following manner: $n^2(0) = \varepsilon_1(0)$. Additionally, the patterns of n (ω) closely resemble $\varepsilon_1(\omega)$. Rb_2CuAsF_6 has the maximum refractive index of 3.0 at 1.80 eV, whereas $Rb_2CuAsCl_6$ shows a refractive index of 2.84 at 1.94 eV and $Rb_2CuAsBr_6$ has 2.88 at 1.60 eV. At an energy of 2.2 eV, the n (ω) value of Rb_2CuAsF_6 is less than one, suggesting that these materials become optically opaque.

In addition, Fig. 8d shows the correlation between the incoming energetic photons and its extinction coefficient k(ω), determined by the equation $2nk = \varepsilon_2(\omega)$ [70], representing the ratio of highest to lowest transmitted energy at a certain energy level. This may be verified by referring to Fig. 4d, where the k(ω) exhibited a similar pattern to the $\varepsilon_2(\omega)$ since both parameters are connected by the Kramer-Kronig relation [37]. The greatest values for k(ω) of Rb_2CuAsF_6, $Rb_2CuAsCl_6$, and $Rb_2CuAsBr_6$ appeared at 2.24 eV, 2.05 eV, and 2.0 eV, respectively.

The optical absorption coefficient α(ω) indicates the potency of the material to capture a certain amount of photon energy. For photovoltaic conversion, the materials need to have a high optical absorption coefficient ($> 10^5$ cm^{-1}) over the whole visible spectrum range. Figure 9a shows the α(ω) spectra of Rb_2CuAsX_6 (X = F, Cl, Br), which display a wide absorption spectrum mainly in the visible-ultraviolet regions, making it well-suited for photovoltaic and optoelectronic devices. Absorption edges are crucial since

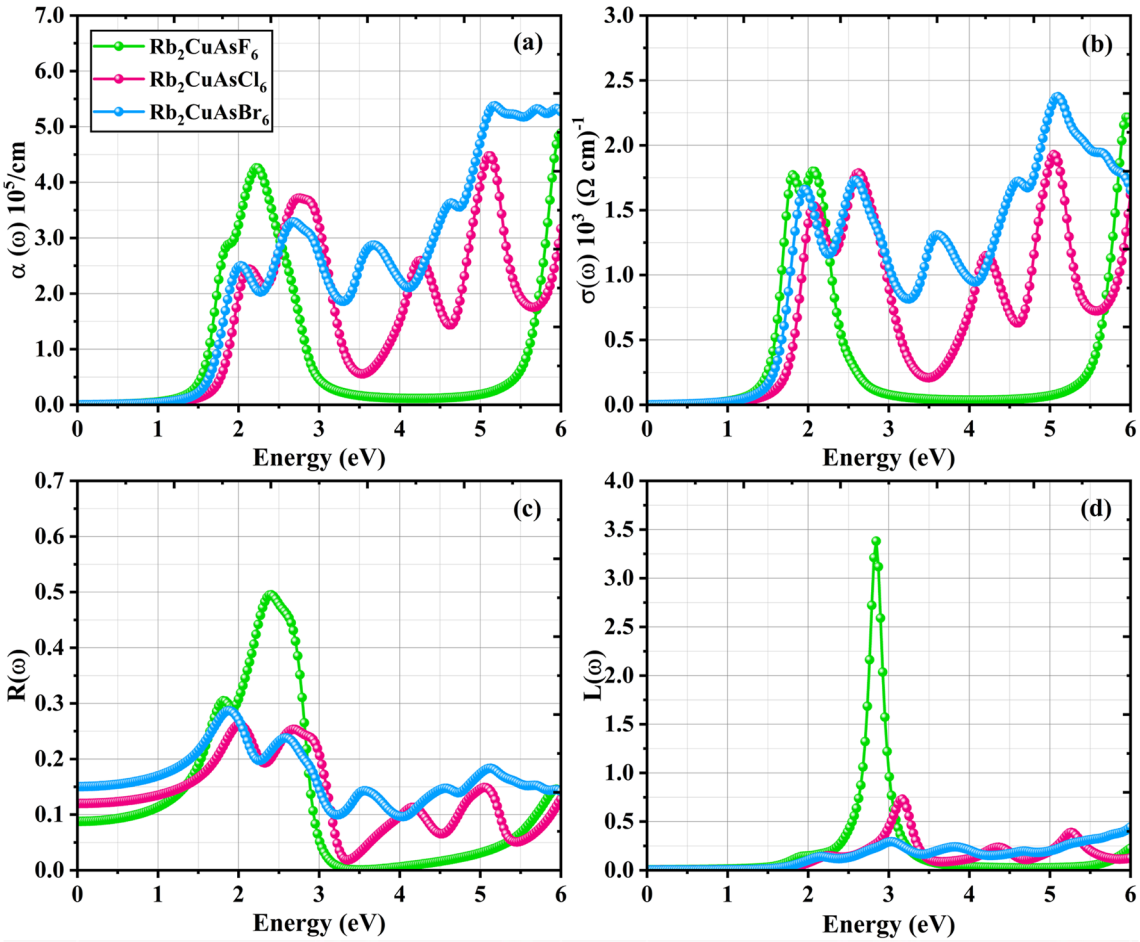

Fig. 9 Variation in optical parameters **a** α(ω) **b** σ(ω) **c** R(ω) **d** L(ω) with energy for Rb_2CuAsX_6 (X = F, Cl, Br)

they indicate the sites at which absorption begins, which are comparable to the band gaps of materials under study. Additionally, there is a significant increase in peak values of 4.4×10^5 cm^{-1}, 3.85×10^5 cm^{-1}, and 3.4×10^5 cm^{-1} when transitioning from Cu-*d* valence states to the unoccupied As-*p* conduction states in the visible region for Rb_2CuAsF_6, $Rb_2CuAsCl_6$, and $Rb_2CuAsBr_6$, respectively. Moreover, the absorption coefficient significantly rises in the UV spectrum for these materials. Based on the band gap energy value and optical absorption spectra, Rb_2CuAsX_6 (X = F, Cl, Br) are well-suited for photovoltaic applications.

Optical conductivity σ(ω) pertains to the bond-breaking mechanism during photon absorption and provides valuable insights into the produced free carriers of energy [71]. The relationship between the energy-dependent σ(ω) pattern and α(ω) is seen in Fig. 9b. In the visible area, Rb_2CuAsF_6, $Rb_2CuAsCl_6$, and $Rb_2CuAsBr_6$ have maximum σ(ω) of 1.79×10^3 $(\Omega\ cm)^{-1}$, 1.62×10^3 $(\Omega\ cm)^{-1}$, and 1.58×10^3 $(\Omega\ cm)^{-1}$, respectively. This demonstrates superior absorption properties of Rb_2CuAsX_6 (X = F, Cl, Br) materials in the visible range. The maximum optical conductivities are reported at the UV region with magnitudes of 2.21×10^3 $(\Omega\ cm)^{-1}$, 2.62×10^3 $(\Omega\ cm)^{-1}$, and 1.93×10^3 $(\Omega\ cm)^{-1}$, respectively. The peak values of Rb_2CuAsF_6, $Rb_2CuAsCl_6$, and $Rb_2CuAsBr_6$ in visible and UV ranges are higher, perhaps due to the carrier density of these materials. The current HDPs exhibit optical activity with an energy spectrum that enhances their use in photovoltaic and optoelectronic technologies, even at high energies.

Optical reflectivity R(ω) is the capacity of a material to deflect incoming photons hitting its exterior. Consequently, when fewer influencing photons are captured, the R(ω) increases significantly [71]. Figure 9c shows the reflectivity of Rb_2CuAsX_6 (X = F, Cl, Br) halide double perovskites. The reflectivity at zero energy R(0) values for Rb_2CuAsF_6, $Rb_2CuAsCl_6$, and $Rb_2CuAsBr_6$ compounds are 8%, 12%, and 15%, respectively. These convey a glimpse into the surface texture of the materials. The visible spectrum shows peak reflectivity values of around 50% for Rb_2CuAsF_6 26%, for $Rb_2CuAsCl_6$, and 28% for $Rb_2CuAsBr_6$. Furthermore, these materials also show weak reflectivity in the UV area, indicating good absorption potency of the materials.

The energy loss factor L(ω) offers valuable insights into the dissipation of optical energy throughout the scattering mechanism when the electron traverses a material or is dissipated by being heated, in addition to absorbance and reflectivity. Figure 9d shows the calculated L(ω) for Rb_2CuAsF_6, $Rb_2CuAsCl_6$, and $Rb_2CuAsBr_6$. Scattering is not detected for photonic energy below band gaps, indicating no energy loss. L(ω) is insignificant for $Rb_2CuAsCl_6$ and $Rb_2CuAsBr_6$, showing peak values of 0.73 and 0.30, respectively, in visible and UV areas, indicating negligible Plasmon losses. However, Rb_2CuAsF_6 exhibits the highest peak value of 3.38 in the visible region, which is significantly higher than $Rb_2CuAsCl_6$, and $Rb_2CuAsBr_6$. Thus, reduced R(ω) and L(ω) improve electrical transport and increase the photoelectric yield of the materials used in photovoltaic (PV) and optoelectronic devices.

3.6 Electron Transport Properties

To address ecological and energy challenges, scientists are focusing on developing efficient thermoelectric components to generate electricity through wasted heat [71, 72]. An effective thermoelectric compound is determined by a figure of merit calculated using the formula: $ZT = S^2\sigma T/k$, where ZT is dependent on factors such as the material's electrical conductivity, heat transfer, and the Seebeck coefficient. Thermoelectric factors including power factor, carrier concentration, Hall coefficient, heat capacity, and figure of merit are analyzed between 100 and 600 K and the relaxation period (τ) is 5×10^{-15} s.

Electrons need to transition from the valence band to the conduction band in order to generate free carriers for n-type materials and holes for p-type materials [73]. Therefore, the charge carrier's mobility is determined by its electrical conductivity (σ/τ), as shown in Fig. 10a. An increase in electrical conductivity is seen in Rb_2CuAsF_6, $Rb_2CuAsCl_6$, and $Rb_2CuAsBr_6$ from (3.29, 2.91, and 2.41×10^{18} $\Omega^{-1}\ m^{-1}\ s^{-1}$) at 100 K to (6.30, 5.30, and 4.94×10^{18} $\Omega^{-1}\ m^{-1}\ s^{-1}$) at 600 K, respectively. The gradual increase in electrical conductivity indicates that the material exhibits semiconductor properties [74]. Moreover, the electrical conductivity at room temperature, shows that Cs2CuAsCl6 (2.51×10^{18} $\Omega^{-1}\ m^{-1}\ s^{-1}$) exhibits better conductivity than $Rb_2CuAsCl_6$ (1.87×10^{18} $\Omega^{-1}\ m^{-1}\ s^{-1}$) and $Rb_2CuAsBr_6$ (1.64×10^{18} $\Omega^{-1}\ m^{-1}\ s^{-1}$). This demonstrates that in solar cells, the heat lost through scattering processes may enhance electrical conductivity, potentially boosting the power conversion efficiency of the solar cells.

The Seebeck coefficient (S) quantifies the voltage generated resulting from the junction of the two distinct materials having different temperatures and influences thermoelectric efficiency [75]. Figure 10c shows that the values of the Seebeck coefficient decrease as temperature increases because of the disruption of atomic bonding. The positive number implies that a large proportion of carriers are holes, categorizing the researched compounds as p-type semiconductors. Rb_2CuAsF_6, $Rb_2CuAsCl_6$, and $Rb_2CuAsBr_6$ compounds have Seebeck values of 271.7 μV K^{-1}, 254.6 μV K^{-1}, and 272.4 μV K^{-1} at 100 K. This value decreases to 209.1 μV K^{-1}, 226.7 μV K^{-1}, and 234.6 μV K^{-1} at 600 K. Subsequently, decrease in S as temperature rises, indicating a steady reduction in the diffusion of agitating charges with increasing temperature [71]. The Seebeck coefficient value of $Rb_2CuAsBr_6$ (263.55 μV K^{-1}) at room temperature

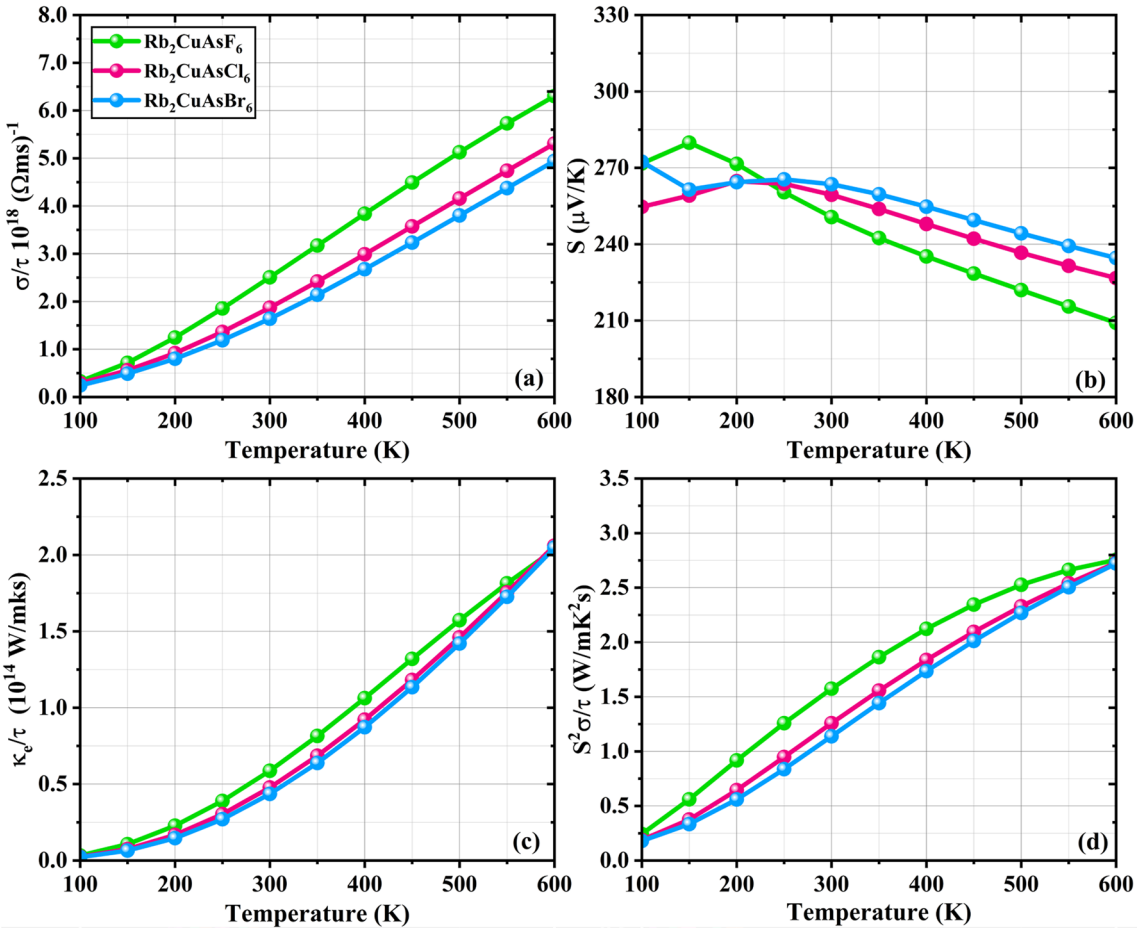

Fig. 10 Variation in transport parameters **a** σ/τ **b** S **c** κ_e/τ **d** $\sigma S^2/\tau$ with temperature for Rb_2CuAsX_6 (X = F, Cl, Br)

is higher than $Rb_2CuAsCl_6$ (259.3 μV K^{-1}) Rb_2CuAsF_6 (250.6 μV K^{-1}).

The thermal conductivity determined by considering just the electrical portion is shown in Fig. 10c. A linear increase in thermal conductivity (κ_e/τ) from 100 to 600 K is observed for all materials. The κ_e/τ for Rb_2CuAsF_6, $Rb_2CuAsCl_6$, and $Rb_2CuAsBr_6$ increases from (3.22, 2.40, and 2.17 × 10^{14} Ω^{-1} m^{-1} s^{-1}) at 100 K to (2.04, 2.06, and 2.05 × 10^{14} Ω^{-1} m^{-1} s^{-1}) at 600 K, respectively. Moreover, Rb_2CuAsF_6 exhibits the highest thermal conductivity of 5.88 × 10^{14} W mks^{-1} at room temperature, followed by $Rb_2CuAsCl_6$ (4.78 × 10^{14} W mks^{-1}), and $Rb_2CuAsBr_6$ (4.36 × 10^{14} W mks^{-1}). These compounds are ideal for thermoelectric devices because of the thermal conductivity differential factor of 10^{-5} from electrical conductivity.

The power factor of a material, crucial for determining its thermoelectric effectiveness, is calculated using the formula $PF = \sigma S^2$, where σ represents electrical conductivity and S is the Seebeck coefficient of materials. The power factor increases with temperature, ranging from (0.24,0.19, and 0.18) × 10^{11} W mK^2s^{-1} at 100 K to (2.76, 2.73, and 2.72) × 10^{11} W mK^2s^{-1} at 800 K in the sequence of Rb_2CuAsF_6 > $Rb_2CuAsCl_6$ > $Rb_2CuAsBr_6$, as seen in Fig. 10d. It is clear that the compounds are sustainable when used at high temperatures since their power factor increases as the temperature rises.

The specific heat capacity (C_v) of materials is formed by charged carriers as well as some phonon contribution. The specific heat capacity for both compounds exhibits a sharp rise with increasing temperature. This rise is in accordance with the Debye model since C_v is proportional to T^3. The value of C_v rises from 0.22 J $molK^{-1}$, 0.09 J $molK^{-1}$, and 0.09 J $molK^{-1}$ to 7.51 J $molK^{-1}$, 2.34 J $molK^{-1}$, and 1.92 J $molK^{-1}$ for Rb_2CuAsF_6, $Rb_2CuAsCl_6$, and $Rb_2CuAsBr_6$. The value of Cv is significantly higher for Rb_2CuAsF_6 than $Rb_2CuAsCl_6$ and $Rb_2CuAsBr_6$ which demonstrates that Rb_2CuAsF_6 has greater capacity of heat absorption.

The carrier concentration (n) is a key parameter to govern the thermal conductivity of a material. Materials having greater carrier concentration might have enhanced electrical conductivity. Figure 11b illustrates a rise in charge concentration from 0.0036 to 0.14 e μc^{-1} for Rb_2CuAsF_6, from

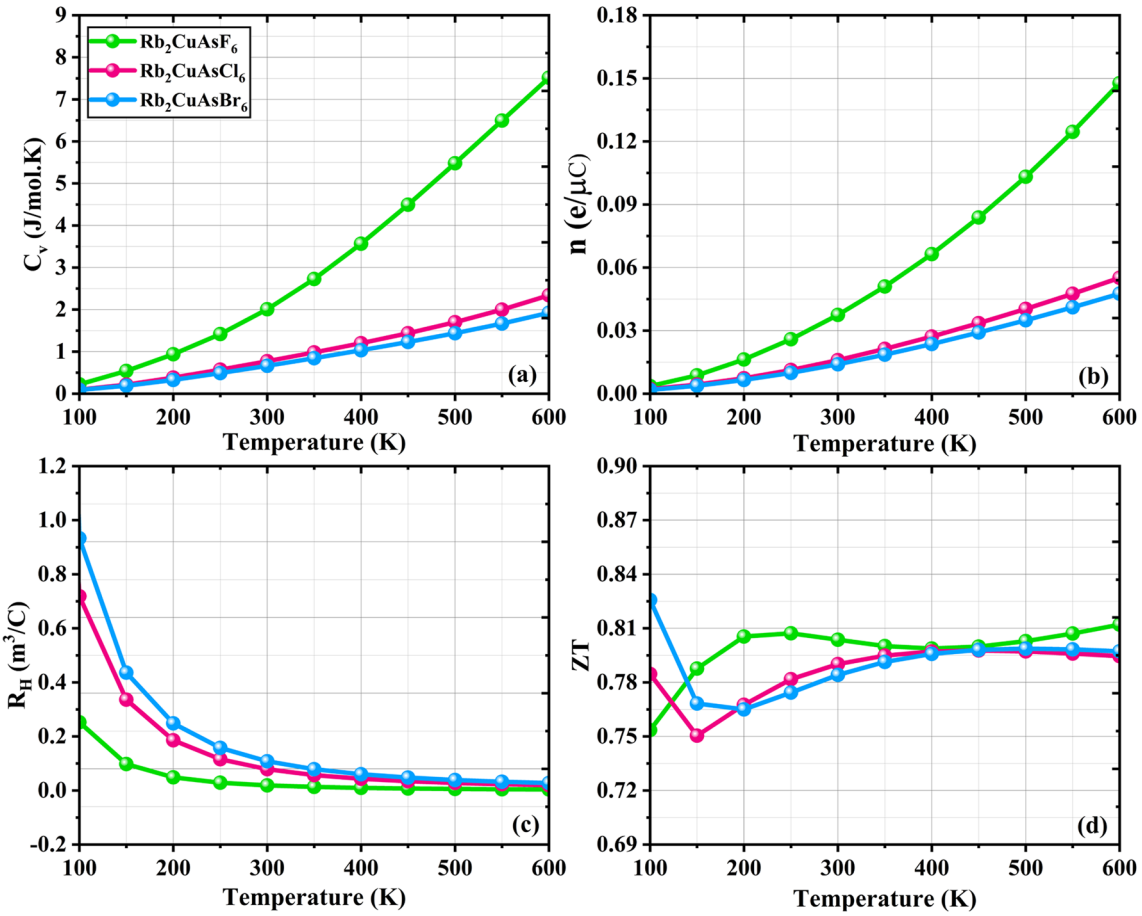

Fig. 11 Variation in transport parameters **a** C_v **b** n **c** R_H **d** ZT with temperature for Rb_2CuAsX_6 (X = F, Cl, Br)

0.0021 to 0.055 e μc^{-1} for $Rb_2CuAsCl_6$, and from 0.0017 to 0.047 e μc^{-1} for $Rb_2CuAsBr_6$ as the temperature rises from 100 to 600 K. This increase in carrier concentration with temperature is attributed to the excitation of charge carriers at elevated temperatures.

The computed Hall coefficient (R_H) at various temperatures for Rb_2CuAsF_6, $Rb_2CuAsCl_6$, and $Rb_2CuAsBr_6$ is displayed in Fig. 11c. This shows that the R_H value is highest at lower temperatures and declines rapidly as the temperature increases, eventually approaching zero for all materials. The Hall Effect is the creation of a current in a semiconductor caused by the presence of opposing charge densities at both sides. Higher temperatures lead to an increase in thermal vibrations which results in increased dispersion and a drop in the values of the Hall coefficient. The positive values of R_H further indicate a p-type semiconductor character of Rb_2CuAsF_6, $Rb_2CuAsCl_6$, and $Rb_2CuAsBr_6$ perovskites.

3.6.1 Figure of Merit

The figure of merit is a crucial characteristic that dictates the effectiveness of thermoelectric systems. Figure 11d illustrates the variation of the figure of merit with temperature up to 600 K for Rb_2CuAsX_6 (X = F, Cl, Br). The ZT = 1 is regarded as the ideal efficiency provided by any material [76]. Throughout the studied temperature range (100–600 K), the ZT value of Rb_2CuAsF_6 and $Rb_2CuAsCl_6$ increases from 0.75 to 0.81 and 0.78 to 0.79, respectively, whereas for $Rb_2CuAsBr_6$, slightly decreases from 0.82 to 0.79. The increased ZT for Rb_2CuAsF_6 and $Rb_2CuAsCl_6$ is justified by greater electrical conductivity and the Seebeck coefficient [77, 78]. Meanwhile, the decrease in ZT for $Rb_2CuAsBr_6$ can be attributed to the increase in heat losses at elevated temperatures [79]. Moreover, at room temperature, Rb_2CuAsF_6, $Rb_2CuAsCl_6$, and $Rb_2CuAsBr_6$ revealed ZT values of 0.80, 0.79, and 0.78, respectively. Our research anticipates the discovery of these new materials with improved thermoelectric performance, making them promising candidates for innovative thermoelectric systems.

4 Conclusion

This work utilized density functional theory (DFT) to evaluate the structural, thermodynamic, elastic, electro-optic, and electron transport characteristics of Rb_2CuAsX_6 (X = F, Cl, Br) perovskites. The substitution of halide ions reveals the variation in mechanical, thermodynamic, optical, and thermoelectric response of studied compounds. The investigation of the elastic parameters and formation energy has confirmed that the examined perovskites are cubic in structure, stable, and ductile. The thermodynamic characteristics revealed the stability at elevated temperatures and suitability for industrial applications. The anisotropy and mechanical strength decrease in the order: $Rb_2CuAsF_6 > Rb_2CuAsCl_6 > Rb_2CuAsBr_6$. The band structure computations identified Rb_2CuAsF_6, $Rb_2CuAsCl_6$, and $Rb_2CuAsBr_6$ are p-type semiconductors with indirect band gaps of 1.25 eV, 1.10, and 0.83 eV, respectively. The values of E_g decrease during the replacement of F with Cl and Br. The optical characteristics demonstrated strong optical absorption and minimal energy loss in the visible and ultraviolet spectrum which highlights their suitability for solar energy conversion. Additionally, thermoelectric characteristics including higher power factor and figure of merit (ZT) values of 0.8, 0.79, 0.78, respectively, at room temperature were determined. Comparatively, Rb_2CuAsF_6 demonstrates superior absorption and ZT values than $Rb_2CuAsCl_6$ and $Rb_2CuAsBr_6$. Our research anticipates these perovskite combinations exhibit superior photoelectric and heat conversion efficiency, rendering them potential prospects for advanced solar cells and thermoelectric devices.

Acknowledgements The authors extend their appreciation to the Deanship of Scientific Research at King Khalid University for funding this work through a large group Research Project under grant number RGP2/358/44. This research was funded by the Princess Nourah bint Abdulrahman University Researchers Supporting Project number (PNURSP2024R7), Princess Nourah bint Abdulrahman University, Riyadh, Saudi Arabia.

Author contributions Ahmad Ayyaz: Conceptualization, Writing-original draft, Review & editing. Figures and Tables G. Murtaza: Formal analysis, Supervision. Youssef Bakkour: Validation, Visualization. Murefah mana Al-Anazy: Data curation, Investigation, Software.

Funding The funding source is not available.

Data Availability The corresponding author will provide the data generated during the study upon a reasonable request.

Declarations

Conflict of interest The authors do not have any known conflict of interest in the publication of this work.

Ethical Approval Not applicable.

References

1. N.S. Lewis, D.G. Nocera, Powering the planet: chemical challenges in solar energy utilization. Proc. Natl. Acad. Sci. **103**(43), 15729–15735 (2006)
2. M. Amin, H.H. Shah, A.G. Fareed, W.U. Khan, E. Chung, A. Zia, Z.U.R. Farooqi, C. Lee, Hydrogen production through renewable and non-renewable energy processes and their impact on climate change. Int. J. Hydrogen Energy **47**(77), 33112–33134 (2022)
3. A. Shah, P. Torres, R. Tscharner, N. Wyrsch, H. Keppner, Photovoltaic technology: the case for thin-film solar cells. Science **285**(5428), 692–698 (1999)
4. K. Maeda, K. Domen, Photocatalytic water splitting: recent progress and future challenges. J. Phys. Chem. Lett. **1**(18), 2655–2661 (2010)
5. D. Beretta, N. Neophytou, J.M. Hodges, M.G. Kanatzidis, D. Narducci, M. Martin-Gonzalez, M. Beekman, B. Balke, G. Cerretti, W. Tremel, A. Zevalkink, Thermoelectrics: from history, a window to the future. Mater. Sci. Eng. **138**, 100501 (2019)
6. H. Zhou, Q. Chen, G. Li, S. Luo, T.B. Song, H.S. Duan, Z. Hong, J. You, Y. Liu, Y. Yang, Interface engineering of highly efficient perovskite solar cells. Science **345**(6196), 542–546 (2014)
7. J. Burschka, N. Pellet, S.J. Moon, R. Humphry-Baker, P. Gao, M.K. Nazeeruddin, M. Grätzel, Sequential deposition as a route to high-performance perovskite-sensitized solar cells. Nature **499**(7458), 316–319 (2013)
8. W.J. Yin, B. Weng, J. Ge, Q. Sun, Z. Li, Y. Yan, Oxide perovskites, double perovskites and derivatives for electrocatalysis, photocatalysis, and photovoltaics. Energy Environ. Sci. **12**(2), 442–462 (2019)
9. Q.A. Akkerman, M. Gandini, F. Di Stasio, P. Rastogi, F. Palazon, G. Bertoni, J.M. Ball, M. Prato, A. Petrozza, L. Manna, Strongly emissive perovskite nanocrystal inks for high-voltage solar cells. Nat. Energy **2**(2), 1–7 (2016)
10. G.E. Eperon, G.M. Paternò, R.J. Sutton, A. Zampetti, A.A. Haghighirad, F. Cacialli, H.J. Snaith, Inorganic caesium lead iodide perovskite solar cells. J. Mater. Chem. A **3**(39), 19688–19695 (2015)
11. T. Krishnamoorthy, H. Ding, C. Yan, W.L. Leong, T. Baikie, Z. Zhang, M. Sherburne, S. Li, M. Asta, N. Mathews, S.G. Mhaisalkar, Lead-free germanium iodide perovskite materials for photovoltaic applications. J. Mater. Chem. A **3**(47), 23829–23832 (2015)
12. P. Ramasamy, D.H. Lim, B. Kim, S.H. Lee, M.S. Lee, J.S. Lee, All-inorganic cesium lead halide perovskite nanocrystals for photodetector applications. Chem. Commun. **52**(10), 2067–2070 (2016)
13. W. Zhang, G.E. Eperon, H.J. Snaith, Metal halide perovskites for energy applications. Nat. Energy **1**(6), 1–8 (2016)
14. X. Wu, High-efficiency polycrystalline CdTe thin-film solar cells. Solar Energy **77**(6), 803–814 (2004)
15. B. Albiss, M. Al-Widyan, Numerical simulation, preparation, and evaluation of Cu (In, Ga) Se_2 (CIGS) thin-film solar cells. ChemEngineering **7**(5), 87 (2023)
16. M.M.A. Moon, M.F. Rahman, J. Hossain, A.B.M. Ismail, Comparative study of the second generation a-Si: H, CdTe, and CIGS thin-film solar cells. Adv. Mater. Res. **1154**, 102–111 (2019)
17 K. Assiouan, A. Marjaoui, J.E. Khamkhami, M. Zanouni, H. Ziani, A. Bouchrit, A. Achahbar, Theoretical investigation of Rb_2AuBiX_6 (X = Br, cl, F) double perovskite for thermoelectric and optoelectronic applications. J. Phys. Chem. Solids **188**, 111890 (2024)
18. T. Leijtens, G.E. Eperon, S. Pathak, A. Abate, M.M. Lee, H.J. Snaith, Overcoming ultraviolet light instability of sensitized

TiO_2 with meso-superstructured organometal tri-halide perovskite solar cells. Nat. Commun. **4**(1), 2885 (2013)
19. A.H. Slavney, R.W. Smaha, I.C. Smith, A. Jaffe, D. Umeyama, H.I. Karunadasa, Chemical approaches to addressing the instability and toxicity of lead–halide perovskite absorbers. Inorg. Chem. **56**(1), 46–55 (2017)
20. A. Babayigit, A. Ethirajan, M. Muller, B. Conings, Toxicity of organometal halide perovskite solar cells. Nat. Mater. **15**(3), 247–251 (2016)
21. M.R. Jani, M.T. Islam, S.M. Al Amin, M.S.U. Sami, K.M. Shorowordi, M.I. Hossain, S. Chowdhury, S.S. Nishat, S. Ahmed, Exploring solar cell performance of inorganic Cs_2TiBr_6 halide double perovskite: a numerical study. Superlatt. Microstruct. **146**, 106652 (2020)
22. L.Z. Lei, Z.F. Shi, Y. Li, Z.Z. Ma, F. Zhang, T.T. Xu, Y.T. Tian, D. Wu, X.J. Li, G.T. Du, High-efficiency and air-stable photodetectors based on lead-free double perovskite $Cs_2AgBiBr_6$ thin films. J. Mater. Chem. C **6**(30), 7982–7988 (2018)
23. M.A. Khan, H.A. Alburaih, N.A. Noor, A. Dahshan, Comprehensive investigation of opto-electronic and transport properties of Cs_2ScAgX_6 (X = Cl, Br, I) for solar cells and thermoelectric applications. Solar Energy **225**, 122–128 (2021)
24. E.T. McClure, M.R. Ball, W. Windl, P.M. Woodward, Cs_2AgBiX_6 (X = Br, Cl): new visible light absorbing, lead-free halide perovskite semiconductors. Chem. Mater. **28**(5), 1348–1354 (2016)
25. Y. Xu, T. Gong, J.N. Munday, The generalized Shockley–Queisser limit for nanostructured solar cells. Sci. Rep. **5**(1), 13536 (2015)
26 A. Ayyaz, G. Murtaza, A. Ahmed, S.M. Ramay, A. Usman, G. Farid, M. Naeem, Comparative DFT-based investigation of physical properties of Cs_2MBiBr_6 (M = Ag, Cu, and Au) Perovskites: sustainable materials for renewable energy. Comput. Condens. Matter. **38**, e00885 (2024)
27. A. Ayyaz, G. Murtaza, M. Umer, A. Usman, H.H. Raza, Structural, elastic, optoelectronic, and transport properties of Na-based halide double perovskites Na_2CuMX_6 (M = Sb, Bi, and X = Cl, Br) as renewable energy materials: a DFT insight. J. Mater. Res. **38**(20), 4609–4624 (2023)
28. A. Ayyaz, G. Murtaza, M. Naeem, A. Usman, S.M. Ramay, M. Irfan, H. Irfan, DFT exploration of elastic, optoelectronic, and thermoelectric properties of stable and eco-friendly double perovskites Cs_2YAuX_6 (X = Cl, Br) for green energy applications. J. Phys. Chem. Solids **188**, 111936 (2024)
29. D.Y. Hu, X.H. Zhao, T.Y. Tang, L.M. Lu, L. Li, L.K. Gao, Y.L. Tang, Exploring the structural, electronic and optical properties of vacancy-ordered double perovskites Cs_2TlAsX_6 (X = I, Br, Cl) based on first-principles. Phys. Lett. A **427**, 127917 (2022)
30. D.Y. Hu, X.H. Zhao, T.Y. Tang, L. Li, Y.L. Tang, Insights on structural, elastic, electronic and optical properties of double-perovskite halides Rb_2CuBiX_6 (X = Br, Cl). J. Phys. Chem. Solids **167**, 110791 (2022)
31. G. Nazir, Q. Mahmood, M. Hassan, Tuning of band gap by anions (Cl, Br, I) of double perovskites Rb_2AgAsX_6 (Cl, Br, I) for solar cells and thermoelectric applications. Phys. Scripta **98**(2), 025811 (2023)
32. S. Charef, A. Assali, A. Boukortt, Optoelectronic and thermoelectric properties of novel double halide perovskites Na_2AgAsX_6 (X = Cl, Br) for efficient green solar cells. Mater. Today Commun. **38**, 108065 (2024)
33. P. Blaha, K. Schwarz, G.K. Madsen, D. Kvasnicka, J. Luitz, wien2k. *An augmented plane wave+ local orbitals program for calculating crystal properties*, *60*(1) (2001)
34. Z. Wu, R.E. Cohen, More accurate generalized gradient approximation for solids. Phys. Rev. B **73**(23), 235116 (2006)
35 G. Rehman, M. Shafiq, Saifullah, R. Ahmad, S. Jalali-Asadabadi, M. Maqbool, I. Khan, H. Rahnamaye-Aliabad, I. Ahmad, Electronic band structures of the highly desirable III–V semiconductors: TB-mBJ DFT studies. J. Electron. Mater. **45**, 3314–3323 (2016)
36. A. Ayyaz, G. Murtaza, M. Shafiq, M.Q. Shah, N. Sfina, S. Ali, Exploring structural, thermodynamic, elastic, electro-optic, and thermoelectric characteristics of double perovskites Rb_2XInBr_6 (X = Na, K) for photovoltaic applications: a DFT approach. Solar Energy **265**, 112131 (2023)
37. V. Lucarini, J.J. Saarinen, K.E. Peiponen, E.M. Vartiainen, *Kramers–Kronig Relations in Optical Materials Research* (Springer, Cham, 2005)
38. G.K. Madsen, D.J. Singh, BoltzTraP. A code for calculating band-structure dependent quantities. Comput. Phys. Commun. **175**(1), 67–71 (2006)
39 A. Otero-de-la-Roza, D. Abbasi-Pérez, V. Luaña, Gibbs A new version of the quasiharmonic model code. II. Models for solid-state thermodynamics, features and implementation. Comput. Phys. Commun. **182**(10), 2232–2248 (2011)
40 J. Tao, J.P. Perdew, H. Tang, C. Shahi, Origin of the size-dependence of the equilibrium van der Waals binding between nanostructures. J. Chem. Phys. (2018). https://doi.org/10.1063/1.5018572
41. G.S. Painter, Improved correlation corrections to the local-spin-density approximation. Phys. Rev. B **24**(8), 4264 (1981)
42. V.G. Tyuterev, N. Vast, Murnaghan's equation of state for the electronic ground state energy. Comput. Mater. Sci. **38**(2), 350–353 (2006)
43. W. Travis, E.N.K. Glover, H. Bronstein, D.O. Scanlon, R.G. Palgrave, On the application of the tolerance factor to inorganic and hybrid halide perovskites: a revised system. Chem. Sci. **7**(7), 4548–4556 (2016)
44. A.E. Fedorovskiy, N.A. Drigo, M.K. Nazeeruddin, The role of Goldschmidt's tolerance factor in the formation of A2BX6 double halide perovskites and its optimal range. Small Methods **4**(5), 1900426 (2020)
45. M.A. Ali, A.A. Alothman, M. Mushab, A. Khan, M. Faizan, DFT insight into structural, electronic, optical and thermoelectric properties of eco-friendly double perovskites Rb_2GeSnX_6 (X = Cl, Br) for green energy generation. J. Inorg. Organometall. Polym. Mater. **33**(11), 3402–3412 (2023)
46. R. Ullah, M.A. Ali, A. Khan, R.A. Alshgari, M.S.S. Mushab, A. Samad, Effect of cation exchange on structural, electronic, magnetic and transport properties of Ba_2MReO_6 (M = In, Gd). J. Magn. Magn. Mater. **546**, 168816 (2022)
47. M.A. Blanco, A.M. Pendás, E. Francisco, J.M. Recio, R. Franco, Thermodynamical properties of solids from microscopic theory: applications to MgF_2 and Al_2O_3. J. Mol. Struct. **368**, 245–255 (1996)
48. E. Francisco, J.M. Recio, M.A. Blanco, A.M. Pendás, A. Costales, Quantum-mechanical study of thermodynamic and bonding properties of MgF_2. J. Phys. Chem. A **102**(9), 1595–1601 (1998)
49. S.A. Dar, V. Srivastava, U.K. Sakalle, V. Parey, Ferromagnetic phase stability, magnetic, electronic, elasto-mechanical and thermodynamic properties of $BaCmO_3$ perovskite oxide. J. Electron. Mater. **47**, 3809–3816 (2018)
50. S.A. Mir, S. Yousuf, D.C. Gupta, First principle study of mechanical stability, magneto-electronic and thermodynamic properties of double perovskites: A_2MgWO_6 (A = Ca, Sr). Mater. Sci. Eng. B **250**, 114434 (2019)
51. S.A. Dar, V. Srivastava, S.N. Tripathi, U.K. Sakalle, A complete DFT description on structural, electronic, elastic, mechanical and thermodynamic properties of some intermetallic AuX_2 (X = Al, Ga, In) compounds. Eur. Phys. J. Plus **133**(12), 541 (2018)
52. J. Luo, A. Yang, Z. Xie, First-principles study on the direct band-gap double perovskite series Cs_2LiInX_6 (X = F, Cl, and Br). ACS Omega **6**(48), 32408–32416 (2021)
53. M.S. Islam, R. Ahmed, M. Mahamudujjaman, R.S. Islam, S.H. Naqib, A comparative study of the structural, elastic,

thermophysical, and optoelectronic properties of $CaZn_2X_2$ (X = N, P, As) semiconductors via ab-initio approach. Results Phys. **44**, 106214 (2023)
54. Z.J. Wu, E.J. Zhao, H.P. Xiang, X.F. Hao, X.J. Liu, J. Meng, Crystal structures and elastic properties of superhard Ir N_2 and Ir N_3 from first principles. Phys. Rev. B **76**(5), 054115 (2007)
55. J.C. Tan, B. Civalleri, C.C. Lin, L. Valenzano, R. Galvelis, P.F. Chen, T.D. Bennett, C. Mellot-Draznieks, C.M. Zicovich-Wilson, A.K. Cheetham, Exceptionally low shear modulus in a prototypical imidazole-based metal-organic framework. Phys. Rev. Lett. **108**(9), 095502 (2012)
56. F. Mouhat, F.X. Coudert, Necessary and sufficient elastic stability conditions in various crystal systems. Phys. Rev. B **90**(22), 224104 (2014)
57. G. Feng, X. Jiang, W. Wei, P. Gong, L. Kang, Z. Li, Y. Li, X. Li, X. Wu, Z. Lin, W. Li, High pressure behaviour and elastic properties of a dense inorganic–organic framework. Dalton Trans. **45**(10), 4303–4308 (2016)
58. S. Kojima, Poisson's ratio of glasses, ceramics, and crystals. Materials **17**(2), 300 (2024)
59. Q. Long, X. Nie, S.L. Shang, J. Wang, Y. Du, Z. Jin, Z.K. Liu, $C_{15}NbCr_2$ laves phase with mechanical properties beyond Pugh's criterion. Comput. Mater. Sci. **121**, 167–173 (2016)
60. C.M. Zener, S. Siegel, Elasticity and anelasticity of metals. J. Phys. Chem. **53**(9), 1468–1468 (1949)
61. Hajjir Titrian, Ugur Aydin, Martin Friák, Duancheng Ma, Dierk Raabe, Jörg. Neugebauer, Self-consistent scale-bridging approach to compute the elasticity of multi-phase polycrystalline materials. MRS Online Proc. Library **1524**, 301–307 (2013)
62. M. Friák, W.A. Counts, D. Ma, B. Sander, D. Holec, D. Raabe, J. Neugebauer, Theory-guided materials design of multi-phase Ti–Nb alloys with bone-matching elastic properties. Materials **5**, 1853–1872 (2012)
63. L.-F. Zhu, M. Friák, L. Lymperakis, H. Titrian, U. Aydin, A.M. Janus, H.-O. Fabritius et al., Ab initio study of single-crystalline and polycrystalline elastic properties of Mg-substituted calcite crystals. J. Mech. Behav. Biomed. Mater. **20**, 296–304 (2013)
64. T. Ou, Q. Zhuang, H. Yan, S. Feng, P. Li, X. Ma, Lead-free halide double perovskites Rb2InSbX6 (X = F, Cl, Br, I): a first-principles study of structural and optoelectrical properties. Chem. Phys. **573**, 112015 (2023)
65. A. Boutramine, S. Al-Qaisi, S. Samah, N. Iram, T.A. Alrebdi, S. Bouzgarrou, A.S. Verma, S. Belhachi, R. Sharma, Optoelectronic and thermoelectric properties of new lead-free K_2NaSbZ_6 (Z = Br, I) halide double-perovskites for clean energy applications: a DFT study. Opt. Q. Electron. **56**(3), 417 (2024)
66. M. Hilal, B. Rashid, S.H. Khan, A. Khan, Investigation of electro-optical properties of InSb under the influence of spin-orbit interaction at room temperature. Mater. Chem. Phys. **184**, 41–48 (2016)
67. M. Gajdoš, K. Hummer, G. Kresse, J. Furthmüller, F.J.P.R.B. Bechstedt, Linear optical properties in the projector-augmented wave methodology. Phys. Rev. B **73**(4), 045112 (2006)
68. G. Grüner, *Electrodynamics of Solids: Optical Properties of Electrons in Matter* (Cambridge University Press, Cambridge, 2002)
69. D.R. Penn, Wave-number-dependent dielectric function of semiconductors. Phys. Rev. **128**(5), 2093 (1962)
70. S. Menakh, B. Daoudi, A. Boukraa, K. Ferkous, First-principles calculations to investigate structural, elastic, electronic and optical properties of A_2OsH_6 for storage hydrogen and optoelectronic devices. Comput. Condens. Matter **31**, e00684 (2022)
71. M.Q. Shah, M. Shafiq, A. Naeem, G. Murtaza, A. Ayyaz, A. Usman, S.M. Deen, M.A. El-Sheikh, Effect of position occupancy of different elements on the structural stability, optoelectronic, thermoelectric and elastic properties of Cs_2CuAsX_6 (X: Cl, Br, I) halide double perovskite: DFT analysis. Mater. Sci. Semicond. Process. **174**, 108187 (2024)
72. S. Hu, Z. Ren, Metal halide perovskites as emerging thermoelectric materials. ACS Energy Lett. **6**(11), 3882–3905 (2021)
73. S.A. Khandy, D.C. Gupta, Electronic structure, magnetism and thermoelectric properties of double perovskite Sr_2HoNbO_6. J. Magn. Magn. Mater. **458**, 176–182 (2018)
74. N.A. Noor, Q. Mahmood, M. Rashid, B.U. Haq, A. Laref, The pressure-induced mechanical and optoelectronic behavior of cubic perovskite $PbSnO_3$ via ab-initio investigations. Ceram. Int. **44**(12), 13750–13756 (2018)
75. G.M. Mustafa, A. Slam, S. Saba, N.A. Noor, M.W. Iqbal, A. Dahshan, Optoelectronic and thermoelectric characteristics of halide based double perovskites K_2YAgX_6 (X = Br, I) for energy storage applications. Polyhedron **229**, 116184 (2023)
76. R.A. Kishore, A. Nozariasbmarz, B. Poudel, S. Priya, High-performance thermoelectric generators for field deployments. ACS Appl. Mater. Interfaces **12**(9), 10389–10401 (2020)
77. G.M. Mustafa, S. Saba, Q. Mahmood, N.A. Kattan, N. Sfina, T. Alshahrani, A. Mera, G.A. Mersal, M.A. Amin, Study of optoelectronic, thermoelectric, mechanical properties of double perovskites Cs_2AgAsX_6 (X = cl, br, I) for solar cells and energy harvesting. Opt. Q. Electron. **55**(6), 527 (2023)
78. J.Y. Al-Humaidi, A. Ullah, N.U. Khan, J. Iqbal, S. Khan, A. Algahtani, V. Tirth, T. Al-Mughanam, M.S. Refat, A. Zaman, First-principle insight into the structural, electronic, elastic and optical properties of Cs-based double perovskites Cs_2XCrCl_6 (X = K, Na). RSC Adv. **13**(30), 20966–20974 (2023)
79. A. Kaltzoglou, P. Falaras, Recent developments on hybrid perovskite materials for solar energy conversion and environmental protection. Current Opin. Chem. Eng. **33**, 100708 (2021)